Flutter/LCO suppression for high-aspect ratio wings

D. Tang **E. H. Dowell**
demant@duke.edu
Department of Mechanical Engineering and Materials Science
Duke University
Durham, NC
USA

ABSTRACT

An experimental high-aspect ratio wing aeroelastic model with a device to provide a controllable slender body tip mass distribution has been constructed and the model response due to flutter and limit cycle oscillations has been measured in a wind tunnel test. A theoretical model has also been developed and calculations made to correlate with the experimental data. Structural equations of motion based on nonlinear beam theory are combined with the ONERA aerodynamic stall model (an empirical extension of Theodorsen aerodynamic theory that accounts for flow separation). A dynamic perturbation analysis about a nonlinear static equilibrium is used to determine the small perturbation flutter boundary which is compared to the experimentally determined flutter velocity and flutter frequency. Time simulation is used to compute the limit cycle oscillations response when the flutter/LCO control system is ON or OFF. Theory and experiment are in good agreement for predicting the flutter/LCO suppression that can be achieved with the control device.

NOMENCLATURE

c, $\bar{c}$	wing chord and dimensionless chord,
c_{SB}	chord of slender body
C_l	section lift coefficient
C_d	section drag coefficient
C_m	section torsional moment coefficient
C_ξ	structural damping
$\mathrm{d}d$,$\mathrm{d}L$	section drag and lift forces
$\mathrm{d}M_0$	section pitch moment about 1/4 chord
$\mathrm{d}F_v$,$\mathrm{d}F_w$	section chordwise and vertical component forces
$\mathrm{d}M_x$	section pitch moment about elastic axis
e	section mass centre from elastic axis
E	modulus of elasticity
g	gravitational constant
G	shear modulus
I_1,I_2	vertical, chordwise area moments
J	torsional stiffness constant
K_m	wing mass radius of gyration
L	wing span
m	mass per unit length of the wing
M	total tip mass of the wing
m_l,m_t	moveable fore-mass and aft-mass of tip slender
N	total number of modes
NN	number of aerodynamic elements
r_m	the controllable position of the movable mass measured from the elastic axis to the mass centre
t	time
U	free stream velocity
v	chordwise or edgewise bending deflection
w	vertical or flapwise bending deflection
V_j,W_j	generalised co-ordinates for bending
x	position co-ordinate along wing span

Paper No. 3307. Manuscript received 17 June 2008, accepted 29 December 2008.

https://doi.org/10.1017/S0001924000003079 Published online by Cambridge University Press

y_{ac} distance of aerodynamic centre of aerofoil section from elastic axis
α_l wing section angle-of-attack
θ_0 steady angle-of-attack at root section
ρ air density
ϕ twist about deformed elastic axis
$\omega_{\phi j}$ jth torsional natural frequency of wing
ω_{vj} jth chordwise natural frequency of wing
ω_{wj} jth vertical natural frequency of wing
Δ_l dimensionless width of lth spanwise aerodynamic element
Φ_j generalised co-ordinates for torsion
$(\,)'$ d( )/dx
$(\dot{})$ d( )/dt

1.0 INTRODUCTION

Uninhabited HALE (high-altitude long-endurance) aircraft are of great current interest. High altitudes and low air densities dictate the use of large wing area and light structural design to increase lift and endurance, thus leading to the design of flexible high aspect ratio wings. These wings undergo large deflections and the geometric structural nonlinearity becomes a very important factor that effects the aeroelastic stability and response of the HALE aircraft. Recent papers[1-8] have shown that there are significant differences between the flutter boundary and limit cycle oscillation (LCO) response computed using a linear structural analysis *vs* a nonlinear structural analysis.

In Refs 6-8, an experimental high-aspect ratio wing aeroelastic model with a tip mass has been constructed and a wind tunnel test conducted to measure the flutter and limit cycle oscillations. The theoretical structural equations of motion are based on nonlinear beam theory[9] and the ONERA aerodynamic stall model[10]. Large static pre-flutter deformations in the vertical or torsional direction are created by the gravity loading on the wing and a tip slender body. Also a steady angle-of-attack creates a static aerodynamic load on the wing.

Following Ref. 6, we construct a new tip slender body whose mass distribution is controllable during flight or a wind tunnel test. Using this tip device the flutter/LCO of the HALE wing has been successfully suppressed. For the new HALE wing model with the controllable tip device, theoretical and experimental studies have been carried out. A dynamic perturbation equation about a nonlinear static equilibrium is derived which is used to determine the flutter boundary. A direct time marching solution is also used to calculate the large amplitude response behaviour of this nonlinear system both above and below the nominal, perturbation flutter boundary, i.e. the flutter boundary determined from the dynamical equations linearised about a nonlinear static equilibrium state. The theoretical results are compared with the measured data from the wing tunnel test. The results provide insight into this flutter/LCO suppression device and its efficacy.

2.0 EXPERIMENTAL WING MODEL AND DEVICE OF TIP MASS DISTRIBUTION CONTROL

The experimental model includes two parts: 1. a high-aspect ratio wing with controllable mass distribution of the slender body at the wing tip and 2. a root support mechanism. The wing is rectangular, untwisted and flexible in the flap, lag and torsional directions. The wing is constructed from a precision ground flat steel spar with mass uniformly distributed along the wing span. The spar is 45·72cm in length, 1·27cm in width and 0·127cm in thickness. It is inserted tightly (clamped) into a wing root mechanism. In order to reduce torsional stiffness, the spar has multiple thin flanges along the span.



Figure 1. Photograph of the experimental model in the wind tunnel.

The flange width is 0·127cm and it is 0·318cm in deep. There are 2 × 33 flanges uniformly and symmetrically distributed along the wing span and centre line of the spar. There are 18 pieces of NACA 0012 aerofoil plate uniformly distributed along the span. The pieces of the aerofoil plate are made of aluminum alloy with 0·254cm thickness. A precision aerodynamic contour of the wing model is obtained. Each aerofoil plate has a slot 1·27cm in width and 0·127cm in thickness at the symmetry line. The spar is inserted through these aerofoil plate slots and they are permanently bonded together. Each space between two aerofoil plates is filled with a light wood (bass) covering the entire chord and span which provides the aerodynamic contour of the wing. This wood provides a slight additional mass and a small addition to the bending and torsion stiffness.

The root support mechanism is a socket that allows a change of the steady angle-of-attack at the root. The root socket is mounted to the mid point of side-wall of the wind tunnel as shown in Fig. 1 which is a photograph of the aeroelastic wing model in the wind tunnel.

Axial strain gauges for bending modes and a 45° oriented strain gage for torsional modes were glued to the root spar to measure the bending-torsional deflections of the wing. Signals from the strain gages were conditioned and amplified before their measurement through a gauge conditioner and a low-pass filter. A micro-accelerometer is mounted at the 1/4 span of the wing. The output signals from these transducers are directly recorded on a computer with data-acquisition and analysis software, Lab-VIEW 8.0.

A slender body with a controllable mass distribution is attached to the elastic axis at the wing tip. The slender body is a strainless steel tube, 0·97cm in inner diameter and 12·44cm (4·9in) in length. Two push type electronic magnetic tubular solenoids, model E-66-38, with 0·95cm diameter are fixed to the two ends of the tube. A parab-oloidal forebody and an aftbody are made of plastic material with 1·14m length and are fixed to the two solenoids. The electronic solenoid is used to create a strong magnet field. The strength of the magnet field is controlled by the external current. The tube in the middle is fixed to the wing span end and the slender body is symmetrical with respect the elastic axis of the wing. Two permanent magnets with 0·95cm in diameter are placed at a position of ±1·5cm measured from the centre of the tube. There is a movable low carbon steel bar (mass) with 0·95cm in diameter and 8·8gram weight placed between the permanent magnet and electronic magnetic tubular solenoid. An extensional spring is connected to the permanent magnet and the movable mass. The position of the movable mass, r_m = 3·56cm, is controlled by the external current. When the power of electronic magnetic tubular solenoid is turned on

https://doi.org/10.1017/S0001924000003079 Published online by Cambridge University Press

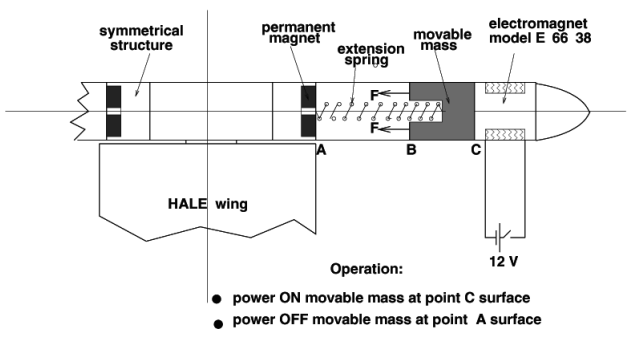


Figure 2. A device configuration for the tip mass distribution control.

(it is called system control OFF), the movable mass is attracted by the solenoid and the position of the mass is at r_m = 3·56cm. This means that there is a larger pitching moment of inertia of the slender body or thus a lower torsional natural frequency of the wing. When the power of electronic magnetic tubular solenoid is turned off (it is called system control ON), the movable mass is attracted by the permanent magnet and the extensional spring. The position of the mass is at r_m = 2·26cm. This means that there is a smaller pitching moment of inertia of the slender body and thus a higher torsional natural frequency of the wing. For details of the tip mass control device, see Fig. 2.

As shown in Fig. 2 when the power of electromagnet set to be on, the movable mass is located at the *C* position due to the electromagnet force being larger then the extension spring force and the permanent magnet force. When flutter/LCO of the HALE wing occurs, the power of the electormagnet automatically turns off (i.e. the system control is ON or the system control is employed). The movable mass automatically moves to the A position due to the extension spring force and a permanent magnet force. Thus flutter/LCO will be suppressed according to the theoretical prediction of the present HALE model. Of course, if it is desired that the movable mass return an other position that is between *A* and *C* position, a variable control of the current of the electromagnet model would be required. The configuration of the tip mass control device is symmetric about the elastic axis of the HALE wing.

All flutter and LCO response tests were performed in the Duke University low-speed wind tunnel. The wind tunnel is a closed circuit tunnel with a test section of 0·7 × 0·53m^2 and a length of 1·52m. The maximum air speed attainable is 89·3ms^{-1}.

The basic parameters of the experimental wing model were obtained from standard static and vibration tests and are listed in Table 1.

Table 1
Experimental wing model data

Wing properties

Span (L)	0·4508m
Chord (c)	0·0508m
Mass per unit length	0·2351kg/m
Mom. Inertia (50% chord)	$0{\cdot}2056 \times 10^{-4}$kgm
Spanwise elastic axis	50% chord
Centre of gravity	49% chord
Flap bending rigidity (EI_1)	0·4186Nm^2
Chordwise bending rigidity (EI_2)	$0{\cdot}1844 \times 10^2$Nm^2
Torsional rigidity (GJ)	0·9539Nm^2
Flap structural modal damping (ξ_w)	0·02
Chordwise structural modal damping (x_v)	0·025
Torsional structural modal damping (ξ_ϕ)	0·031

Slender body properties

Radius (R)	$0{\cdot}4762 \times 10^{-2}$m
Chord length (c_{SB})	0·1406m
Total mass (M)	0·053kg
moveable mass (m_l, m_t)	0·0088, 0·0088kg
Moment of inertia (I_{x0})	$0{\cdot}629 \times 10^{-4}$kgm^2
Moment of inertia (I_y)	$0{\cdot}4546 \times 10^{-6}$kgm^2
Moment of inertia (I_{z0})	$0{\cdot}629 \times 10^{-4}$kgm^2
Total (I_x)	$I_x = I_{x0} + (m_l + m_t)r_m^2$
Total (I_x)	$I_z = I_x$

3.0 NONLINEAR AND SMALL PERTURBATION FLUTTER EQUATIONS

3.1 Structural model

According to the Hodges-Dowell equations[9], for an uniform, untwisted elastic wing, neglecting cross-section warping, the equations of motion may be written as

$$\begin{aligned} &EI_2 v'''' + (EI_2 - EI_1)(\phi(w)'')'' \\ &+m\ddot{v} + C_\xi \dot{v} + (M\ddot{v} + I_v \ddot{v}')\delta(x-L) \\ &= \frac{dF_v}{dx} + \Delta F_v - (Mg\delta(x-L) + mg)\mathrm{Sin}\theta_0 \end{aligned} \quad \ldots (1)$$

$$\begin{aligned} &EI_1(w)'''' + (EI_2 - EI_1)(\phi v'')'' + m\ddot{w} \\ &-me\ddot{\phi} + C_\xi \dot{w} + (M\ddot{w} + I_w \ddot{w}')\delta(x-L) \\ &= \frac{dF_w}{dx} + \Delta F_w - (Mg\delta(x-L) + mg)\mathrm{Cos}\theta_0 \end{aligned} \quad \ldots (2)$$

$$\begin{aligned} &-GJ\phi'' + (EI_2 - EI_1)w''v'' \\ &+I_\phi \ddot{\phi}\delta(x-L) + mK_m^2\ddot{\phi} + C_\xi\dot{\phi} - me\ddot{w} \\ &= M_{move} + \frac{dM_x}{dx} + \Delta M_x \end{aligned} \quad \ldots (3)$$

where M_{move} is a static pitch moment about the elastic axis created by the moveable masses in the slender body.

$$M_{move} = (m_l r_{ml} + m_t r_{mt})g\delta(x-L)$$

where r_{ml} and r_{mt} are distances between elastic axis and the masses m_l and m_t, respectively. The effects of m_l and m_t are also included in M, I_v, I_w and I_ϕ of course.

A few general comments about Equations (1)-(3) may be in order. First of all by multiplying each of these equations by δv, δw and $\delta\phi$ respectively and integrating over the length of the beam, a variational statement may be derived. Conversely as shown in Ref. 9, these equations may be derived from Hamilton's principle.

Note that in Equations (1)-(3) only the most important nonlinear terms are retained from the Hodges-Dowell equations and the third and higher order geometrically nonlinear terms are neglected here. Also note that the geometric twist angle $\hat{\phi} = \phi + \int_0^x v'w''dx$ is considered in the aerodynamic terms. M is the tip mass and I_v, I_w and I_ϕ are the tip inertial terms, and θ_0 is the pitch angle or steady angle-of-attack at the root of this wing model. e is the distance between mass centre and wing elastic axis centre.

https://doi.org/10.1017/S0001924000003079 Published online by Cambridge University Press

The aerodynamic forces include two parts. One contribution is from the wing surface $\frac{dF_w}{dx}, \frac{dF_v}{dx}$ and $\frac{dM_x}{dx}$, and the other is from the slender body at the wing tip, ΔF_w, ΔF_v and ΔM_x.

3.2 Part one (ONERA aerodynamic aerofoil model)

The v and w components of the aerodynamic force, and the aerodynamic moment about the elastic axis can be expressed as follows.

$$dF_w = dL - (\phi_\lambda - \theta_0)dD$$

$$dF_v = -dD - (\phi_\lambda - \theta_0)dL \quad \ldots (4)$$

$$dM_x = dM_0 - y_{ac}dF_w$$

where

$$dL = \frac{1}{2}\rho c U^2 C_l dx$$

$$dD = \frac{1}{2}\rho c U^2 C_d dx$$

$$dM_0 = \frac{1}{2}\rho c^2 U^2 C_m dx$$

$$\phi_\lambda \approx \dot{w}/(U + \dot{v} + \dot{w}\theta_0)$$

$$\alpha = \hat{\phi} + \theta_0 - \phi_\lambda$$

The section aerodynamic coefficients C_l, C_d and C_m are obtained from the original ONERA stall aerodynamic model. These aerofoil relationships are combined with a strip theory assumption to determine the wing aerodynamic forces. Patil *et al*[10] have shown the strip theory assumption is a good one for such high aspect ratio wings.

3.3 Part two (slender body theory)

We follow a book[11] written by Bisplinghoff, Ashley and Halfman, p 418 *et seq*. Using essentially the nomenclature of the book[11], we define $h = w_{x=L}$, $\alpha = \phi_{x=L}$, $L = \Delta F_w$, $M_x = \Delta M_x$ but use the symbol y to denote chordwise position. Then the vertical displacement at the wing tip is

$$Z_a = -h - \alpha[y - y_B] \quad \ldots (5)$$

where $y_B \equiv y_{ea}$, is the distance from leading edge to the elastic axis of the slender body. Here h, + up, and α, + nose up. Now the downwash or convected vertical velocity is

$$W_a = \frac{\partial Z_a}{\partial t} + U\frac{\partial Z_a}{\partial y} = \frac{DZ_a}{Dt} \quad \ldots (6)$$

where $D \equiv \frac{\partial}{\partial t} + U\frac{\partial}{\partial y}$

Thus,

$$\frac{dL}{dy} = -\rho\frac{DS}{Dt} - \rho S\frac{D^2 Z_a}{Dt^2} = -\rho\frac{D}{Dt}[S\frac{DZ_a}{Dt}] \quad \ldots (7)$$

where $S \equiv$ body cross-sectional area and $S = \pi R^2$, for a circular cross-section of radius, $R(y)$.

Note that $\frac{DS}{Dt} = U\frac{dS}{dy}$ $\ldots (8)$

Then Equation (7) becomes

$$\frac{dL}{dy} = -\rho U\frac{dS}{dy}\frac{DZ_a}{Dt} - \rho S\frac{D^2 Z_a}{Dt^2} \quad \ldots (9)$$

Now, $L \equiv \int_0^{c_{SB}} \frac{dL}{dy}dy$ and $M_x \equiv \int_0^{c_{SB}} \frac{dL}{dy}[y - y_B]dy$

where c_{SB} chord of slender body.

Using Equation (5),

$$\frac{DZ_a}{Dt} = -\dot{h} - \dot{\alpha}[y - y_B] - U\alpha$$

$$\frac{D^2 Z_\alpha}{D^2 t} = -\ddot{h} - \ddot{\alpha}[y - y_B] - 2U\dot{\alpha}$$

thus

$$\Delta F_w = L \equiv \int_0^{c_{SB}} \frac{dL}{dy}dy = \rho[\ddot{h} + U\dot{\alpha}]\int_0^{c_{SB}} S dy + \rho\ddot{\alpha}\int_0^{c_{SB}} S[y - y_B]dy \quad \ldots (10)$$

and

$$\Delta M_x = M_x \equiv -\int_0^{c_{SB}} \frac{dL}{dy}[y - y_B]dy = \rho U[\dot{h} + U\alpha]\int_0^{c_{SB}} S dy - \rho\ddot{h}\int_0^{c_{SB}} S[y - y_B]dy - \rho\ddot{\alpha}\int_0^{c_{SB}} S[y - y_B]^2 dy \quad \ldots (11)$$

Note that $\int_0^{c_{SB}} \frac{dS}{dy}dy = -\int_0^{c_{SB}} S dy$ if $S = 0$ at $y = 0$, c_{SB}, i.e. for a pointed body.

Also, recall the sign convention is y- positive aft, L- positive up and M_x- positive nose up.

If we assume the slender body drag can be neglected, then

$$\Delta F_v = -(\phi_\lambda - \phi - \theta_0)\Delta F_w \quad \ldots (12)$$

3.4 Modal equations

Expansions in general mode shape functions are used to obtain ordinary differential equations in terms of generalised co-ordinates from Equations (1)-(3). They are expressed in series form as follows.

$$\bar{v} = \sum_{j=1}^{N} V_j(t)\psi_j(\bar{x})$$

$$\bar{w} = \sum_{j=1}^{N} W_j(t)\psi_j(\bar{x}) \quad \ldots (13)$$

$$\phi = \sum_{j=1}^{N} \Phi_j(t)\Theta_j(\bar{x})$$

where the over-bar indicates non-dimensionalisation with respect to the wing span, L, and ψ_j, Θ_j are the jth normal modes of the associated linear structural model.

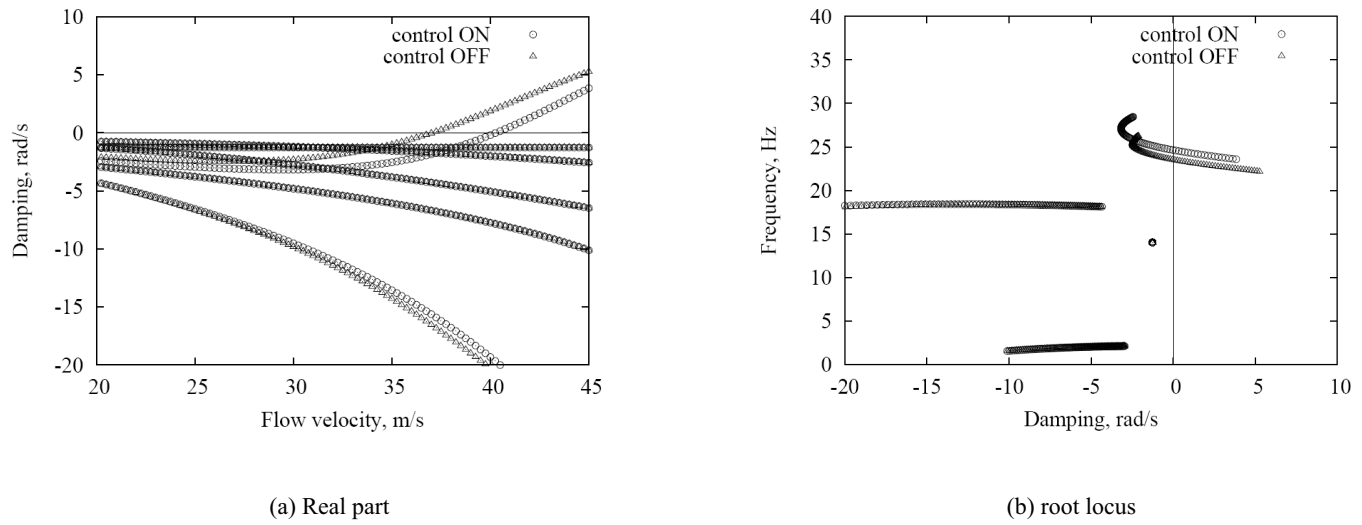
Let **{q}** be a state vector which is defined as

$$\{\mathbf{q}\} = \{\dot{V}_j, V_j, \dot{W}_j, W_j, \dot{\Phi}_j, \Phi_j, C_{ll}, C_{ml}, C_{dl}\}$$

where the structural mode number is j = 1, 2, ...N, and the aerodynamic section number along the span of the wing is l = 1, 2, ...NN. Using the Galerkin method, one obtains a set of state-space matrix equations from Equations (1)-(4) and (13),

$$[A]\{\dot{q}\} + [B]\{q\} = \{F_0\} + \{F_N\} \quad \ldots (14)$$

https://doi.org/10.1017/S0001924000003079 Published online by Cambridge University Press



(a) Real part (b) root locus

Figure 3. Perturbation eigenvalue solution of the nonlinear aeroelastic system for $\theta_0 = 1°$, (a) real part of eigenvalue and (b) root locus.

Note the coefficient matrices, [**A**], [**B**] are dependent on the flow and structural parameters. The force vectors F_N and F_0 are the static forces obtained from the effects of gravity and the nonlinear forces obtained from the structural nonlinearity and stall aerodynamics, respectively.

Equation (14) is a set of nonlinear equations of motion. A strictly linear flutter boundary is determined using Equation (14) by setting $F_N \equiv 0$ and $F_0 = 0$. There is no effect on the strictly linear flutter boundary of a pre-flutter static deflection or initial conditions. For $F_N \neq 0$ and a large static pre-flutter deformation, a dynamic perturbation approach is used to determine the small perturbation flutter boundary of this nonlinear system about a nonlinear and non-trivial static equilibrium condition. That is, one assumes that

$$q = \bar{q} + \hat{q} \qquad \ldots (15)$$

where $\bar{q}$ is the static equilibrium state variables and the corresponding quantities with a symbol of (^) are the small (linear) dynamic perturbations about the static equilibrium state.

Substituting Equation (15) into Equation (14), a set of static equilibrium equations and dynamic perturbation equations is obtained. The static equilibrium equations comprise a set of nonlinear algebraic equations for the unknown state vector $\{\bar{\mathbf{q}}\}$

The dynamic perturbation equations about a static equilibrium state are

$$[\bar{A}]\{\dot{\hat{q}}\} + [\bar{B}]\{\hat{q}\} = \{0\} \qquad \ldots (16)$$

Note the coefficient matrices, $[\bar{\mathbf{A}}]$, $[\bar{\mathbf{B}}]$ are dependent on the flow velocity and the static equilibrium state, e.g. U, $\bar{q}$ etc.

To determine the dynamic nonlinear response of this aeroelastic system, we can use Equation (14) and a time marching approach.

A note on the sign convention may be helpful here. Vertical bending deflection, w, and the direction of gravity are taken as positive up. Chordwise bending deflection, v, is taken as positive aft. And the torsional deflection and angle-of-attack are taken positive nose up. Note that since gravity is positive up, we are flying the wing upside down and, for example, a negative angle-of-attack is required to provide a lift downward to balance the wing weight.

4.0 CORRELATION BETWEEN THEORY AND EXPERIMENT

The correlation study focuses on flutter/LCO suppression *per se*. For a detailed investigation of nonlinear aeroelastic effects on flutter/LCO[1-8]. The theoretical and experimental model is set to an initial pitch angle, $\theta_0 = 1°$, and the wing structural parameters are the same as those in Ref. 6. However, the structural parameters of tip slender body in the present paper are slightly different from those in Ref. 6.

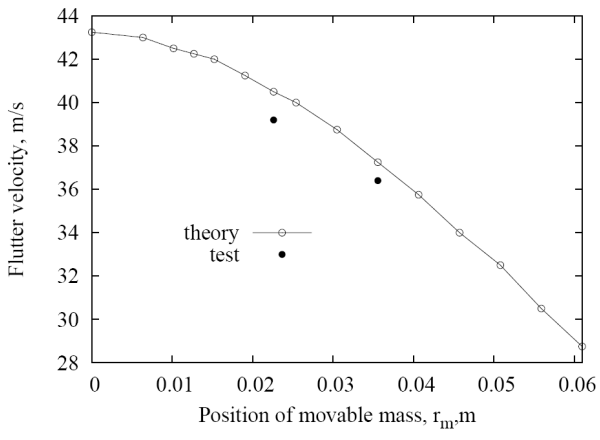
The theoretical results are obtained from the dynamic perturbation Equation (16) and also using a time marching approach for the full nonlinear Equations (14).

Figure 3(a),(b) show a graphical representation of the perturbation equations eigenanalysis in the form of real eigenvalues $\mathrm{Re}(\lambda_i)$ (damping) vs the flow velocity and also a root-locus plot (frequency *vs* damping) as indicated by the symbol Δ for $r_m = 3{\cdot}56$cm and by the symbol ◦ for $r_m = 2{\cdot}26$cm. These conditions correspond to the system control OFF ($r_m = 3{\cdot}56$cm) and the system control ON ($r_m = 2{\cdot}26$cm). There is a intersection of $\mathrm{Re}(\lambda_i)$ with the velocity axis at $U_f = 37{\cdot}2\mathrm{ms}^{-1}$ and the corresponding flutter oscillatory frequency is $\omega_f = 23{\cdot}46$Hz for $r_m = 3{\cdot}56$cm and $\theta_0 = 1°$. For $r_m = 2{\cdot}26$cm, the flutter velocity and frequency are the $U_f = 40{\cdot}5\mathrm{ms}^{-1}$ and $\omega_f = 24{\cdot}52$Hz. This means the flutter velocity increases significantly when the movable masses move forward to wing elastic axis only by 1·3cm. This is because the pitching moment of inertia of the tip slender body decreases and the torsional natural frequency increases when the movable masses move forward to wing elastic axis. The theoretical and experimental results show flutter velocity and frequency are sensitive to the torsional natural frequency of the HALE wing.

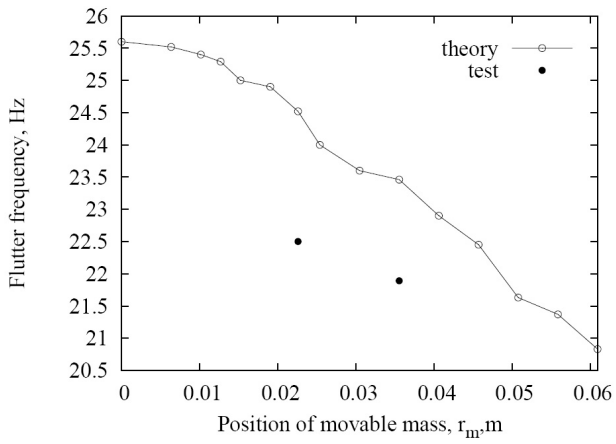
Figure 4 shows the dynamic perturbation flutter velocity (a) and frequency (b) *vs* the position, r_m, of the movable masses, m_l and m_t from nonlinear theory. The initial pitch angle θ_0 is 1°. The solid line is for the dynamic perturbation theory and the symbol, •, is for test. For the flutter velocity, the agreement is good and the error is less than 3%. For the flutter frequency, the agreement is reasonable and the error is less than 9%.

Figure 5 (a) (b) shows the theoretical LCO time histories (a) for the 1/4-span flapwise deflection and (b) for twist deflection at tip for

https://doi.org/10.1017/S0001924000003079 Published online by Cambridge University Press

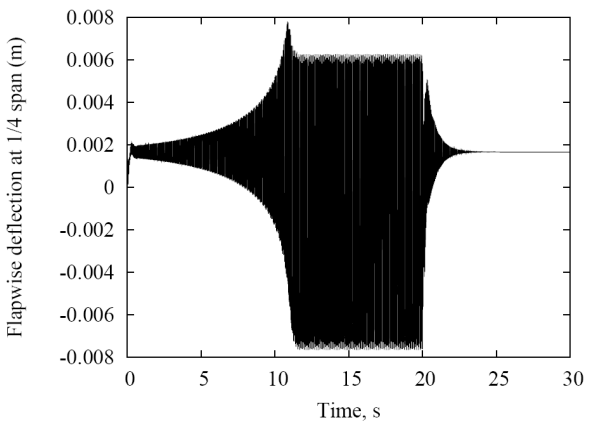


(a) Flutter velocity

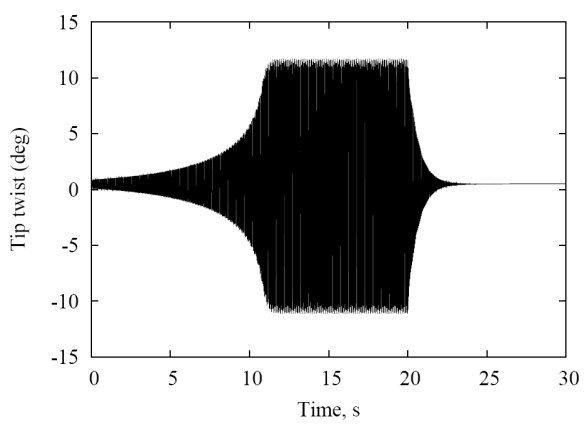


(b) Flutter frequency

Figure 4. Nonlinear theoretical flutter velocity and frequency *vs* the position of movable masses, m_l and m_t for $\theta_0 = 1°$ and comparison with test results.



(a) 1/4 span flapwise deflection



(b) Tip twist

Figure 5. Theoretical time history for $U = 37{\cdot}5 ms^{-1}$ and $\theta_0 = 1°$, (a) 1/4-span flapwise deflection (b) tip twist.

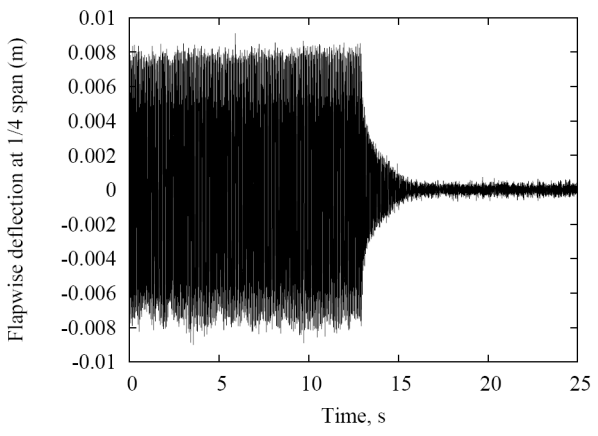
flow velocity $U = 37{\cdot}5 ms^{-1}$ and $\theta_0 = 1°$. From Fig. 5, we find the stall aerodynamic nonlinearity leads to a limit cycle oscillation before 20 seconds using r_m = 3·56cm. At t = 20+ Δt seconds, we set r_m = 2·26cm, i.e. the tip mass control device is employed. The LCO response decays to a static equilibrium position and LCO disappears. The decay time is about 2·5 seconds from the maximum LCO amplitude. As seen from Fig. 5(b), the twist deflection reaches about 12 degrees and the actual angle of attack is larger than the dynamic stall angle. Stall aerodynamics is a major factor that leads to the LCO response.

Figure 6 (a) (b) shows the experimental LCO time histories (a) for the 1/4-span flapwise deflection from t = 1 to 25 seconds, and (b) for an expanded time scale representation of the decay response for a flow velocity of $U = 37{\cdot}5 ms^{-1}$ and $\theta_0 = 1°$. From Fig. 6, we see the tip mass control activated at 12·8 seconds. After this time the LCO amplitude decays to a small amplitude. The rms amplitude is about 0·0008 (m). From the FFT analysis of this small response, the PSD has a random behaviour which is due to the wind-tunnel turbulence. Figure 6(b) shows the decay response, the experimental decay time is about three seconds. Comparing Fig. 5 to Fig. 6, the experimental results are seen to be close to the theoretical results.

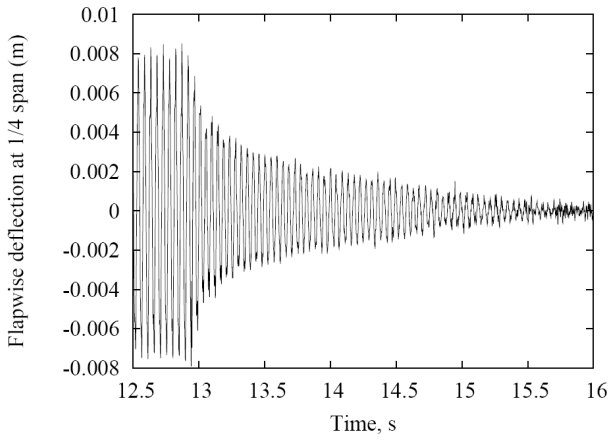
Figure 7 shows a comparison between theoretical and experimental FFT analysis for flapwise deflection at the 1/4-span for $U = 37{\cdot}5 ms^{-1}$ and $\theta_0 = 1°$. The motion includes two dominant frequency components, a first harmonic and a second harmonic. The first harmonic is 23·53Hz from the theory and 21·48Hz from test which corresponds to the fundamental flutter frequency. The second harmonic is 43Hz from test and 47Hz from theory. The response is dominated by the first harmonic flutter frequency. The agreement between theory and experiment is reasonably good.

A typical plot of LCO amplitude and frequency for r_m = 3·56cm (without tip mass control), $\theta_0 = 1°$ and at the 1/4 span position is shown in Fig. 8. The theoretical and experimental amplitudes are taken as rms average values from a 50 second sampling interval. The symbols, ◦ and •, indicate the experimental results obtained by increasing or decreasing flow velocity, respectively. The solid and broken lines (without symbols) indicate the theoretical results for increasing and decreasing flow velocity, respectively. For the increasing flow velocity case, the theoretical limit

https://doi.org/10.1017/S0001924000003079 Published online by Cambridge University Press



(a) 1/4 span flapwise deflection



(b) detail of decay response

Figure 6. Experimental time history for $U = 37{\cdot}5\text{ms}^{-1}$ and $\theta_0 = 1°$, (a) 1/4-span flapwise deflection (b) detail of decay response.

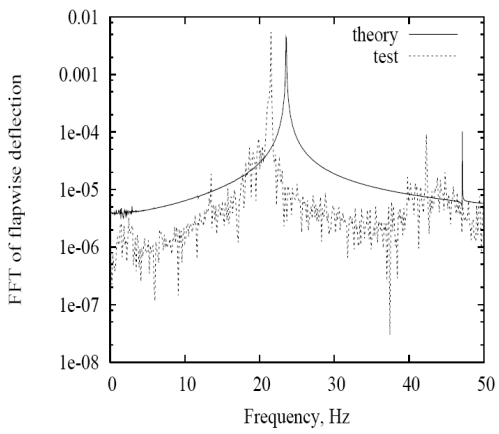


Figure 7. Theoretical and experimental FFT analysis for $r_m = 3{\cdot}56\text{cm}$, $U = 37{\cdot}5\text{ms}^{-1}$.

cycle oscillation occurs when the flow velocity is larger than the perturbation flutter velocity and the amplitude has a jump from almost rest to a larger value. Once the onset of LCO occurs, the amplitude increases smoothly with increasing the flow velocity. When $U > 40{\cdot}5\text{ms}^{-1}$, a numerical or possibly a physical divergence is found in the theoretical model. For the case of decreasing flow velocity, as shown by the broken line, the LCO amplitude decreases but does not exactly coincide with those obtained by the increasing velocity case. Also there is a jump in the LCO response at $U = 36{\cdot}5\text{ms}^{-1}$ which is a distinctly lower velocity than that found for the increasing velocity case (i.e. $U = 37{\cdot}5\text{ms}^{-1}$). Thus hysteresis is found in both the theoretical and experimental results.

Figure 9 (a) (b) show the theoretical and experimental LCO time histories for the 1/4-span flapwise deflection (a) for theory and (b) for test for a flow velocity of $U = 41{\cdot}0\text{ms}^{-1}$ and $\theta_0 = 1°$. The tip movable mass position is at $r_m = 2{\cdot}26\text{cm}$, i.e the tip mass control device is active from time $t = 0$ until $t = 20$ seconds. The corresponding FFT analysis for these theoretical and experimental results is shown in Fig. 10. The theoretical LCO frequency is higher than the one from the test. Agreements between theory and test for both LCO amplitude and frequency is reasonably good.

5.0 CONCLUSION

The present experimental and theoretical results provide new insights into nonlinear aeroelastic phenomena and flutter/LCO suppression for high aspect ratio wings with a tip mass distribution control device. The present control system and device are effective for the suppression of flutter/LCO. This study also shows the effects of the geometric structural nonlinearity as modeled by nonlinear beam theory and nonlinear aerodynamic stall theory on both the flutter instability boundary and the nonlinear limit cycle oscillation response. The onset of a limit cycle oscillation is dependent upon a delicate balance between nonlinear stall aerodynamics and the structural nonlinear forces. However, the stall aerodynamics are responsible for hysteresis in the present experimental wing model.

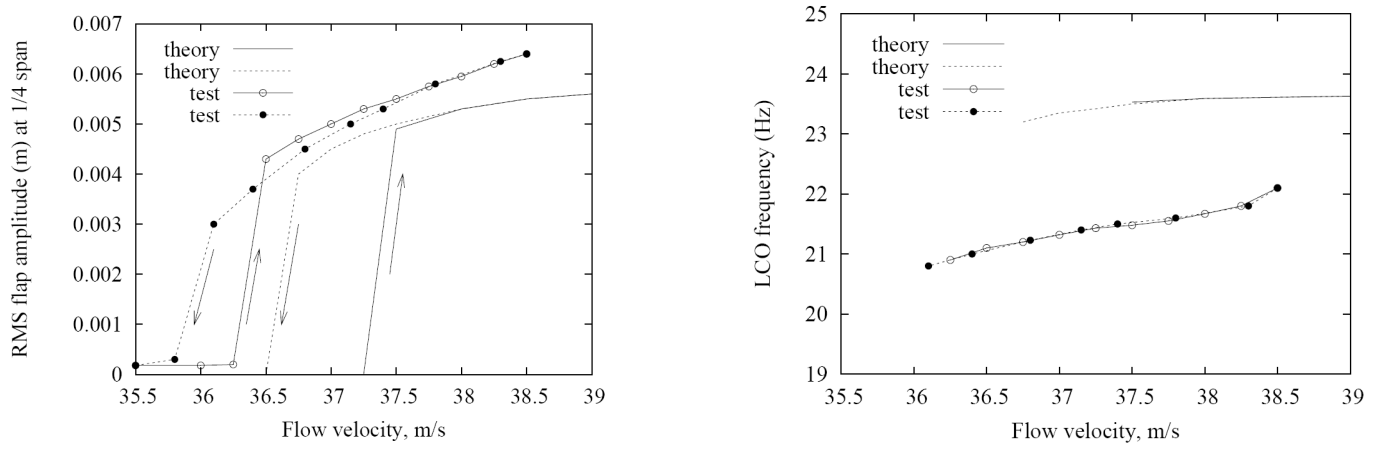
ACKNOWLEDGMENTS

This work was supported under AFOSR Grant, 'Physics-Based Identification, Modeling and Management Infrastructure for Aeroelastic Limit-Cycle Oscillations', under the direction of Dr Victor Giurgiutiu. We would also like to thank our colleague, Professor Henri P. Gavi, for his assistance in the design in the control system.

REFERENCES

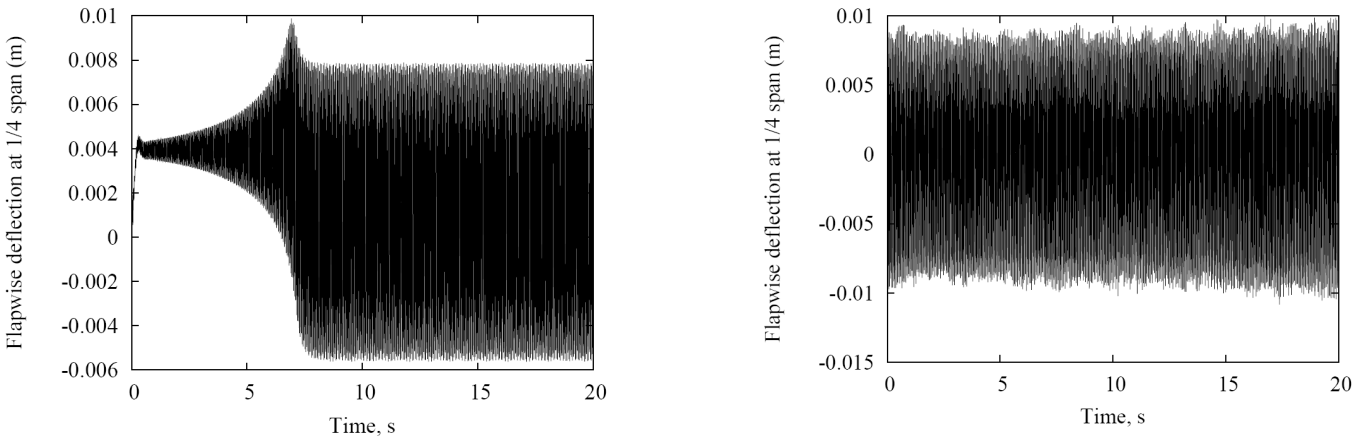
1. VAN SHOOR, M.C. and VON FLOTOW, A.H. Aeroelastic characteristics of a highly flexible aircraft, *J Aircr*, 1990, **27**, (10), pp 901-908.
2. PATIL, M.J., HODGES, D.H. and CESNIK, C.E.S. Limit cycle oscillations in high-aspect-ratio wings, AIAA Paper-99-1464.
3. PATIL, M.J. and HODGES, D.H. On the importance of aerodynamic and structural geometric nonlinearities in aeroelastic behavior of high-aspect-ratio wings, April 2000, AIAA Paper 2000-1448.
4. TANG, D.M. and DOWELL, E.H. Effects of geometric structural nonlinearity on flutter and limit cycle oscillations of high-aspect ratio wings, *J Fluids and Structures*, 2004, **19**, (34), pp 291-306.
5. GARCIA, J.A. Numerical investigation of nonlinear aeroelastic effects on flexible high-aspect-ratio wings, *J Aircr*, 2005, **42**, (4), pp 1025-1036.
6. TANG, D.M. and DOWELL, E.H. Experimental and theoretical study on aeroelastic response of high-aspect ratio wings, *AIAA J*, 2001, **39**, (8), pp 1430-1441.
7. TANG, D.M. and DOWELL, E.H. Experimental and theoretical study of gust response for a high-aspect ratio wing, *AIAA J*, 2002, **40**, (3), pp 419-429.

https://doi.org/10.1017/S0001924000003079 Published online by Cambridge University Press



(a) LCO amplityde (b) LCO frequency

Figure 8.Theoretical and experimental LCO amplitude (a) and LCO frequency (b) *vs* flow velocity for $\theta_0 = 1°$ and r_m = 3·56cm.



(a) theory (b) test

Figure 9. Theoretical and experimental LCO time histories 1/4-span flapwise deflection, for U = 41ms^{-1}, $\theta_0 = 1°$ and r_m = 2·26cm.

8. TANG, D.M. and DOWELL, E.H. Limit cycle hysteresis response for a high-aspect ratio wing model, *J Aircr*, 2002, **39**, (5), pp 885-888.
9. HODGES, D.H. and DOWELL,E.H., Nonlinear equations of motion for the elastic bending and torsion of twisted nonuniform rotor blades, NASA TN D-7818, 1974.
10. TRAN, C.T. and PETOT, D. Semi-empirical model for the dynamic stall of airfoils in view to the application to the calculation of responses of a helicopter blade in forward flight, *Vertica*, 1981, **5**, (1), pp 35-53.
11. BISPLINGHOFF, R.L., ASHLEY, H. and HALFMAN, R.L. *Aeroelasticity*, 1955, Addison-Wesley.

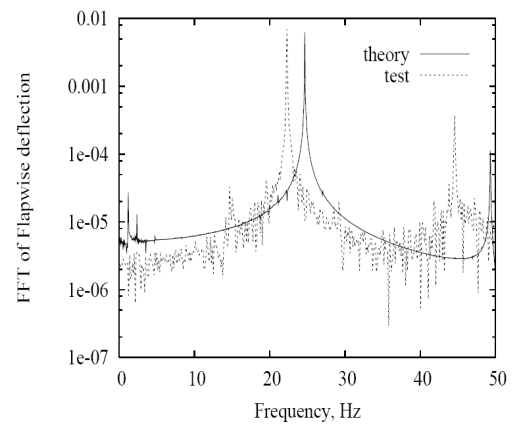


Figure 10. Theoretical and experimental FFT analysis for U = 41ms^{-1}, $\theta_0 = 1°$ and r_m = 2·26cm.

https://doi.org/10.1017/S0001924000003079 Published online by Cambridge University Press